Inorganic Chemistry
Article
pubs.acs.org/IC

Facile Oxidative Conversion of TiH_2 to High-Concentration Ti^{3+}-Self-Doped Rutile TiO_2 with Visible-Light Photoactivity

Lauren R. Grabstanowicz,[†,∥] Shanmin Gao,[†] Tao Li,[‡] Robert M. Rickard,[†] Tijana Rajh,[§] Di-Jia Liu,[∥] and Tao Xu*,[†]

[†]Department of Chemistry and Biochemistry, Northern Illinois University, DeKalb, Illinois 60115, United States

[‡]Advanced Photon Source, [§]Center for Nanoscale Materials, and [∥]Chemical Science and Engineering, Argonne National Laboratory, Argonne, Illinois, United States, 60439

ABSTRACT: TiO_2, in the rutile phase with a high concentration of self-doped Ti^{3+}, has been synthesized via a facile, all inorganic-based, and scalable method of oxidizing TiH_2 in H_2O_2 followed by calcinations in Ar gas. The material was shown to be photoactive in the visible-region of the electromagnetic spectrum. Powdered X-ray diffraction (PXRD), transmission electron microscopy (TEM), ultraviolet−visible-near-infrared (UV−vis-NIR), diffuse reflectance spectroscopy (DRS), and Brunauer−Emmett−Teller (BET) methods were used to characterize the crystalline, structural, and optical properties and specific surface area of the as-synthesized Ti^{3+}-doped rutile, respectively. The concentration of Ti^{3+} was quantitatively studied by electron paramagnetic resonance (EPR) to be as high as one Ti^{3+} per ~4300 Ti^{4+}. Furthermore, methylene blue (MB) solution and an industry wastewater sample were used to examine the photocatalytic activity of the Ti^{3+}-doped TiO_2 which was analyzed by UV−vis absorption, Fourier transform infrared spectroscopy (FT-IR), and electrospray ionization mass spectrometry (ESI-MS). In comparison to pristine anatase TiO_2, our Ti^{3+} self-doped rutile sample exhibited remarkably enhanced visible-light photocatalytic degradation on organic pollutants in water.

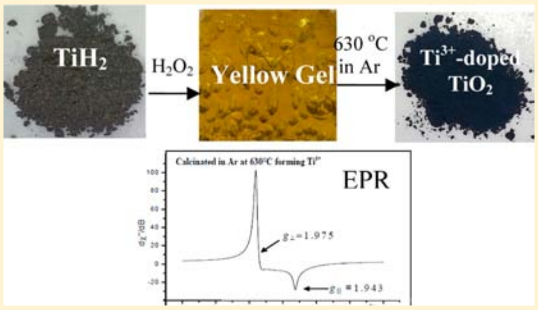

INTRODUCTION

Titanium dioxide (TiO_2) is one of the most promising photocatalysts due to its light, thermal, and electrochemical stabilities.[1−3] However, the large band gap of pure TiO_2 (~3.2 eV) renders it only active in the ultraviolet (UV) region. Thus, only UV light (<5% of total solar energy) can be utilized to generate electron−hole pairs for the desired photoelectrochemical (PEC) processes.[4−9] To significantly improve the photocatalytic efficiency, it is therefore crucial to enhance the light harvesting of TiO_2 in the visible spectrum, which accounts for ~43% of the total solar energy. One of the current strategies to tackle this challenge is through band gap reduction engineering via doping various metal cations, such as Ag, Nd, Sb, Ru, V, Cr, Mn, and Fe,[10,11] or nonmetal elements, such as S, I, C, etc.,[12,13] in TiO_2. Such processes introduce impurity states into the TiO_2 band gap to enhance visible-light harvesting. However, issues such as the environmental hazards from dopant leaching, lower efficiency from dopant-induced charge recombination and/or traps, and dopant-induced thermal instability pose some significant limitations.[14]

Recently, incorporating Ti^{3+} and/or oxygen vacancies in TiO_2 has emerged as an effective approach to introduce visible photoactivity with a reduced environmental impact.[15−19] However, theoretical work has suggested that, in order to achieve an efficient activity in the visible spectrum, the concentration of Ti^{3+} must be sufficiently high to induce a continuous vacancy band of electronic states just below the conduction band edge of TiO_2.[20] Otherwise, a low Ti^{3+} doping concentration only creates localized oxygen vacancy states that deteriorate the electron mobility and exhibit a negligible visible photoactivity. This is due to the fact that the energy of the scattered doping states is largely (0.75−1.18 eV) below the conduction band edge of TiO_2 and the occupying photoelectrons are not adequately reactive and/or mobile for desired electrochemical reactions.[21,22] Therefore, doping a high concentration of Ti^{3+} in TiO_2 is essential to enhance the photocatalytic activity in the visible region.

To date, however, only a handful of methods are capable to produce Ti^{3+} and/or oxygen vacancy doped TiO_2. These methods all start from pure TiO_2, from which a fraction of the Ti^{4+} ions is reduced to Ti^{3+} under harsh, costly, and often complicated conditions, such as thermal reduction at high pressure (>20 bar) in reducing gases (H_2 or CO)[15,16,18] or bombardment with a high energy laser, electron, or Ar^+ beams.[3] These methods are generally considered impractical for a large scale commercial production. Furthermore, since the reduction occurs mainly on the surface of TiO_2, the oxygen vacancies are usually not adequately thermally stable, even when in air. The Ti^{3+} ions could also be easily oxidized over a short period of time by dissolving oxygen found in water.[23,24] Thus, there is a pressing need to develop a facile synthetic strategy to achieve a

Received: November 29, 2012
Published: March 18, 2013

dx.doi.org/10.1021/ic3026182 | *Inorg. Chem.* 2013, 52, 3884−3890

high-concentration of Ti^{3+} doping throughout the bulk TiO_2 matrix with improved thermal and chemical stabilities.

We report herein a transformative method of preparing a highly active, yet stable TiO_2 containing a high concentration of Ti^{3+} embedded inside a rutile matrix. In contrast to current solid-state reduction-based methods, we applied a solution-based, oxidative approach to generate Ti^{3+} species that are uniformly distributed throughout the bulk of the resulting TiO_2 matrix. The first key to this innovative chemistry is to choose TiH_2 as the starting material. TiH_2 is a widely used industrial commodity in the powder metallurgy industry.[25]

Because the oxidation state of the titanium species in TiH_2 is +2, a controllable oxidative agent is needed to convert part of the Ti^{2+} species to Ti^{3+} species. This oxidative conversion of $Ti^{2+} \rightarrow Ti^{3+}$ is fundamentally different from the reported reductive conversion of $Ti^{4+} \rightarrow Ti^{3+}$. To control the oxidation process and to avoid any unnecessary contaminations, the second key to this innovation is to choose H_2O_2 as the oxidation agent. Consequently, the only byproduct that needs to be removed is H_2O and/or H_2. At ambient temperatures, TiH_2 is highly stable in air and water but very reactive with peroxides.[26] Such a solution-based oxidative method could lead to a scalable and low cost production of highly efficient Ti^{3+} self-doped TiO_2 photocatalyst within the existing industrial infrastructure.

As shown in Scheme 1, by reacting gray TiH_2 powders with a 30% aqueous solution of H_2O_2, the TiH_2 powder was gradually converted to a yellow or green gel-like product, presumably forming a cross-linked $[-O-Ti-O-]_n-Ti-(OH)_x \cdot mH_2O$ matrix, but with substantial oxygen vacancies. This gel was then desiccated followed by calcination in Ar under an optimal temperature in order to remove moisture and form a TiO_2 lattice with substantial Ti^{3+}. In this way, dopants can be obtained throughout the bulk of the TiO_2 matrix.

Scheme 1. [a]

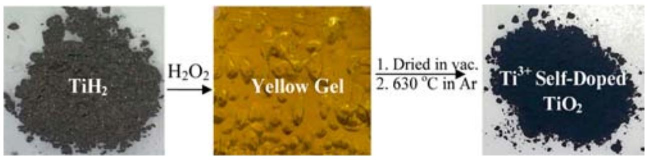

[a] Images of gray TiH_2 powder, which was converted to yellowish gel after reaction with H_2O_2. The gel was further heated to yield the black TiO_2 powder.

■ EXPERIMENTAL DETAILS

Experimental Synthesis of Ti^{3+}-Self-doped TiO_2. Titanium(II) hydride (TiH_2, 99.0%) and hydrogen peroxide (H_2O_2, 30.0%) were both purchased from Aldrich without further purification. A typical procedure for preparing the Ti^{3+} self-doped TiO_2 powder sample is described as follows: First, 10 mL of distilled water was added to 0.96 g of TiH_2 and sonicated for 10 min to form a suspension. Then, 15 mL of H_2O_2 was added to the mixture and continuously stirred for 3 h at room temperature. At this point, the solution began to coagulate and became a miscible gel-like slurry. Then, 12 mL H_2O_2 was added and the mixture was stirred for 4 h followed by adding another 15 mL of H_2O_2 and stirring for 16 h. A yellow gel was thus obtained. However, if the starting TiH_2 had been exposed to air for some time, the gel turned to a greenish color. The gel was then vacuum-desiccated overnight to remove most of the moisture. The sample was then placed in an oven at 100 °C for 12−20 h, until the gel sample was converted into a yellow powder. The yellow powder sample was then calcinated at 630 °C for 3 h in Ar, which led to the production of a very black Ti^{3+} self-doped TiO_2 powder. The overall synthesis is depicted in Scheme 1. The as-synthesized Ti^{3+} self-doped TiO_2 black powder was then ball-milled (SPEX 8000 M Mixer/Mill) with dried yttria-stabilized zirconia beads (2.0 mm) and NaCl powder (400 mesh) for 1 h at 10 min intervals. Upon completion, the sample was then rinsed with distilled water and filtered. Filterization was performed until the filtrate, with flame colored test, no longer indicated to have a yellow−orange color, in order to ensure the removal of NaCl.

Structural Characterization. Powder X-ray diffraction (PXRD) patterns of the final products were obtained on a Rigaku D/max-2500VPC with a Ni-filtered Cu Kα radiation at a scan rate of 0.02° s^{-1} from 20° to 60°. X-band continuous wave electron-paramagnetic resonance (EPR) experiments were carried out using a Bruker ELEXSYS E580 spectrometer operating in the X-band (9.4 GHz) and equipped with an Oxford CF935 helium flow cryostat with an ITC-5025 temperature controller. The g factors were calibrated by comparison to a coal standard, $g = 2.00285(\pm 0.00005)$. The first-derivative EPR spectra were recorded at 5 K in the dark. The surface area and pore size distribution data were obtained by measuring nitrogen sorption isotherms at 77 K on a Micromeritics ASAP 2020 surface area and pore size analyzer. Pore size distribution was calculated using a nonlinear density functional theory (NLDFT) model, which is available in the Micromeritics ASAP 2020 software package (assuming slit pore geometry). Before the measurements, samples were degassed at 180 °C overnight. Ultrahigh purity N_2 was used for all measurements. Transmission electron microscope (TEM) was conducted with a FEI Tecnai F20ST TEM/STEM using an accelerating voltage of 200 kV. Thermogravimetric analysis (TGA) was performed on a Perkin-Elmer, model Pyris 1 system in open air. Ultraviolet−visible-near-infrared (UV−vis-NIR) diffuse reflectance spectra (DRS) were recorded on a Perkins Elmer Lambda 950 spectrophotometer.

Analysis of Photocatalytic Activity. A methylene blue solution was first prepared to model the organic wastewater for the surface adsorption and for a photoactivity evaluation. The concentration of the methylene blue was determined by monitoring the changes in the maximal absorbance at approximately $\lambda = 650$ nm characterized by a UV−vis spectrometer (Ocean Optics Inc.). In each test, approximately 0.05 g of catalyst was added to ~30 mL of a methylene blue solution and sonicated for 5 min. Then, the suspension was magnetically stirred for 30 min until an adsorption−desorption equilibrium was established. The degradation process was performed under illumination at 1 sun 1.5 a.m. G provided by a solar simulator (Photo Emission Inc. CA, model SS50B). For the UV−vis analysis of the MB solution and wastewater, during photocatalytic reaction, 3 mL aliquots were collected at selected time intervals. In order to separate the catalyst from the solution, the mixture was centrifuged for three 20 min intervals. The mass spectra (MS) were taken on an electrospray ionization mass spectrometer (ESI-MS) using a Bruker ESQUIRE 3000. Fourier transform-infrared (FT-IR) spectra were recorded on a MAGNA 550 FT infrared spectrometer on samples embedded into KBr pellets.

■ RESULTS AND DISCUSSION

The powder X-ray diffraction (PXRD) analysis was used to investigate the crystal structure of the raw materials (TiH_2), intermediate (gel after desiccation but before calcination), and the samples after calcination in Ar under 530 and 630 °C (Figure 1). The commercial TiH_2 is typically in the fcc $TiH_{1.971}$ crystal phase (δ phase). Prior to calcination, the gel was vacuum desiccated and oven-dried at 100 °C to yield a yellowish powder. The XRD pattern indicated that the intermediate powder was a fairly amorphous blend of both anatase and rutile. Upon calcinations under 530 °C in Ar, the sample structure became rutile-dominated as seen in spectrum c of Figure 1. The diffraction peaks associated with TiH_2 were also completely removed after calcination. A further temperature increase to

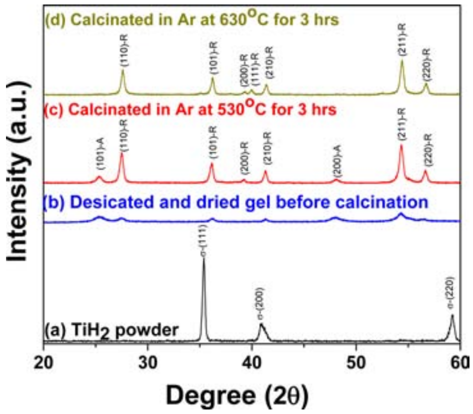

Figure 1. XRD patterns of (a)TiH_2; (b) desiccated gel (a yellow powder) prior to calcination; (c) $Ti^{3+}-TiO_2$ calcinated at 530 °C in Ar; and (d) $Ti^{3+}-TiO_2$ calcinated at 630 °C in Ar (A = anatase; R = rutile).

630 °C led to the formation of pure rutile in spectrum d of Figure 1. The strong diffraction peaks at $2\theta = 27.6°$, 36.1°, 41.1°, and 54.4° can be indexed to the (110), (101), (111), and (211) crystal planes of rutile TiO_2, respectively (PDF card 75-1755, JCPDS). Recent work suggests that the coexistence of both (110) and (111) crystal faces in rutile TiO_2 promotes the photogenerated electron transfer from (111) to (110) face. Thus, the (110) face of rutile TiO_2 acts as reductive sites, while the (111) face serves as oxidative sites.[27] Although anatase TiO_2 typically is more photoactive than rutile, recent studies have indicated, in the case of Ti^{3+}self-doped TiO_2, that the rutile structure is more photoactive than anatase.[28]

Low temperature electron paramagnetic resonance (EPR) was conducted to identify and quantify the presence of Ti^{3+}. Figure 2a shows the EPR spectrum at 4.2 K of the sample obtained after H_2O_2 oxidation and annealing in Ar at 630 °C. Two major features in this spectrum, both belonging to Ti^{3+}, are in an axially symmetric environment. The g values of these features are consistent with the perpendicular and parallel components of the axially symmetric lattice Ti^{3+} centers in the rutile environment with $g_\perp = 1.975$ and $g_\| = 1.943$, respectively.[29,30] This finding suggests that the Ti^{3+} centers obtained via our method are located in the bulk lattice of the resulting rutile crystal. The amount of Ti^{3+} centers obtained by annealing for 3 h is quite large, 5.7×10^{17} spins/g (4.6×10^{19} spins/mol), indicating that one in every 4.3×10^3 Ti atoms was converted to Ti^{3+}. When the same sample was annealed in air, all Ti^{3+} centers were oxidized to Ti^{4+}. No paramagnetic species in the region of $g < 2$ was observed (see Figure 2b), confirming disappearance of the reducing species of Ti^{3+} upon heating in oxygen. Instead, a signal characteristic of superoxide radical species obtained by interaction of H_2O_2 with TiO_2 or by reaction with molecular oxygen was detected.[31,32] Interestingly, when citric acid instead of H_2O_2 was used to mix with TiH_2 followed by annealing in Ar at 630 °C, the resulting sample exhibits a broad signal for Ti^{3+} species. This broad peak is an indication of the surface centered radicals that are experiencing distribution of coordination environments. Therefore, a range of g values averaging at 1.999, 1.965, and 1.948 that were previously attributed to Ti^{3+} surface species in rutile are present.[33] The annealing also resulted in incomplete oxidation of organic (citric acid) to carbonaceous material with carbon centered radicals with $g = 2.0028$ (the same g value as coal samples), suggesting that oxidation of organics in inert atmosphere proceeds via reactions involving electron transfer to rutile surfaces. These electrons are significantly less stable than lattice trapped electrons and react easily with electron scavengers such as oxygen or N_2O. Here the number of Ti^{3+} centers is much smaller as only 3.8×10^{15} spins/g were observed, suggesting that one in every 6.6×10^5 Ti atoms is reduced. We believed our oxidative method incorporates Ti^{3+} in the inner lattice of TiO_2, whereas the reduction method is mainly on the surface where oxygen can escape. Hence, EPR unambiguously verified the presence and amount of Ti^{3+} within our self-doped samples.

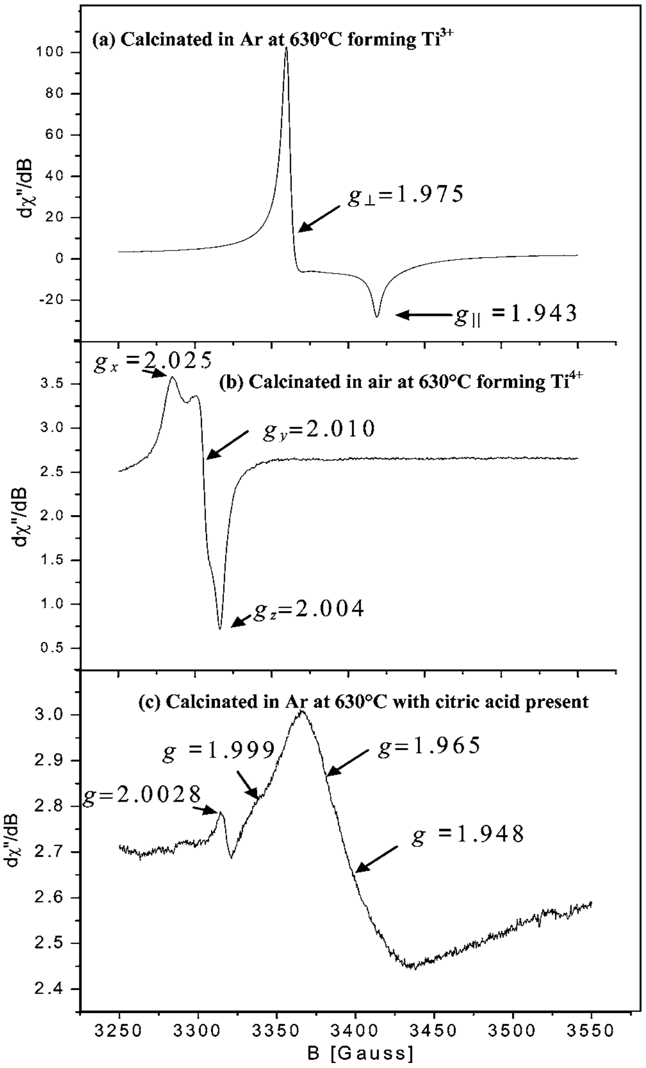

Figure 2. EPR spectra of (a) Ti^{3+}-doped TiO_2 calcinated in Ar at 630 °C, (b) Ti^{4+} presence when calcinated in open air at 630 °C, and (c) calcination in Ar at 630 °C with use of citric acid.

The thermal stability of the sample annealed at 630 °C was further studied by TGA in open air, as is shown in Figure 3. The sample was thermally stable up to 180 °C in open air with a negligible weight variation. This also suggests that the Ti^{3+} species are located in the bulk of the crystal instead of on the crystal surface, in agreement with the EPR results. Above 180 °C, the sample weight increases, indicating the oxygen uptake by the Ti^{3+} species.

Transmission electron microscope (TEM) was used to further examine the particle size, crystallinity, and morphology

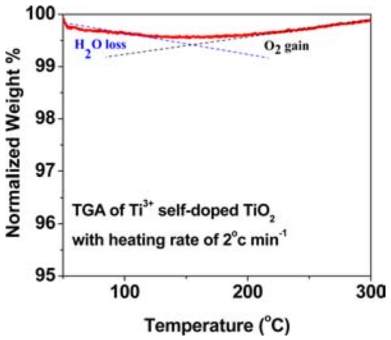

Figure 3. TGA curve in open air for Ti^{3+}-self-doped TiO_2 sample that was calcinated at 630 °C in Ar.

of the samples. TEM images of Ti^{3+}-self-doped TiO_2 nanopowders calcinated at 530 and 630 °C are shown in Figure 4. Figure 4a shows that the particle sizes of the sample treated at 530 °C are typically around 200 nm. As the calcination temperature was raised to 630 °C, the average particle size increased to 400 nm as shown in Figure 4b. This is presumably due to the sintering of the particles at higher temperature. Figure 4c and d is the high-resolution TEM (HRTEM) images of the sample calcinated at 530 and 630 °C, respectively, of which the lattices were clearly observed, indicating these particles were highly crystallized. The samples calcinated at 530 °C shows the lattice spacings of $d = 0.352$ and 0.325 nm which could be attributed to the (101) plane of the anatase phase and the (110) plane of the rutile phase, respectively, suggesting that the sample is a mixture of both phases.[34,35] In addition, the samples calcinated at 630 °C shows the lattice spacing of d = 0.324 nm, in agreement with the (110) atomic plane of the rutile TiO_2.

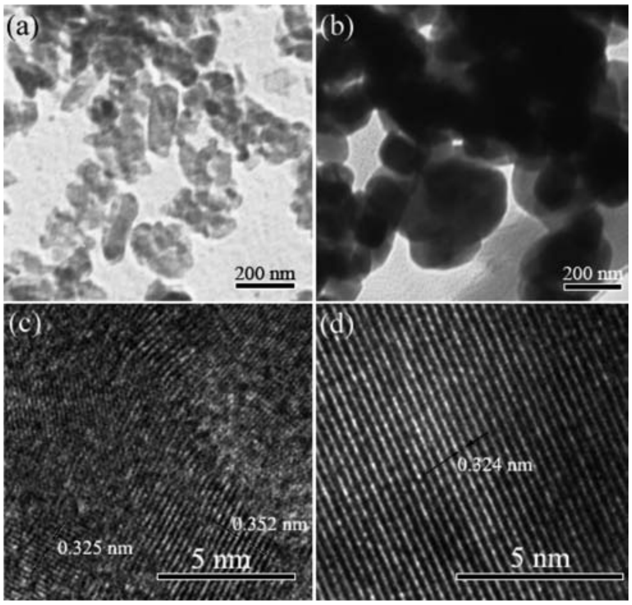

Figure 4. (a and b) TEM image of the obtained samples with heat treatment at 530 and 630 °C for 3 h under argon atmosphere, respectively. (c and d) HRTEM images for sample a and b, respectively.

For photocatalysts, increasing porosity and specific surface area have been shown to improve photocatalysis efficiency.[36,37] The porosities of the ball-milled (BM) and nonball-milled (NBM) Ti^{3+}-doped TiO_2 sample (calcinated at 630 °C) were measured using BET method at 77 K. A type-II hybrid isotherm was found in both samples, as indicated in Figure 5a, which represents a standard isotherm for a nonporous or macroporous adsorbent. Furthermore, the loop around $1.0P/P_0$ for both samples was determined to be a type-H3 loop. This type of loop is observed with an agglomeration of platelike particles resulting in slit-shaped pores, concurring with the HRTEM images in Figure 4d. The apparent pore width distributions of the samples are also evident in Figure 5b based on NLDFT calculation. A distinct difference between the BM and NBM sample is found. The NBM, with a BET surface area of 2.33 m^2 g^{-1}, has a pore width distribution from mesopore to macropore with the range of 20−120 nm. On the other hand, the BM sample quadrupled the BET surface area up to 8.16 m^2 g^{-1}. Furthermore, Figure 5b shows the pore size distributed in both meso/macroporous (>20 nm) and micro/mesoporous regions (<3 nm). We should also point out that the sample became noticeably darker indicating an increase of pore volume and surface area after ball-milling.

The optical property of the Ti^{3+}-self-doped TiO_2 powder sample was analyzed by UV−vis-NIR, as is shown in Figure 6. A commercial pristine anatase was also analyzed for comparison. The absorption region of the Ti^{3+}-self-doped TiO_2 sample exhibits a significant redshift (from 330 to 370 nm) of the peak in the UV region when compared with the commercial anatase (see Figure 6 inset). Most importantly, the Ti^{3+}-self-doped TiO_2 sample also displays a broad absorbance in the visible region between 400 and 800 nm. Furthermore, the absorption band of the sample extends into the near-IR region. This agrees with the assumption that there is a subband located just below the conduction band edge of pure TiO_2 due to the high-concentration of Ti^{3+}.[15,18,20]

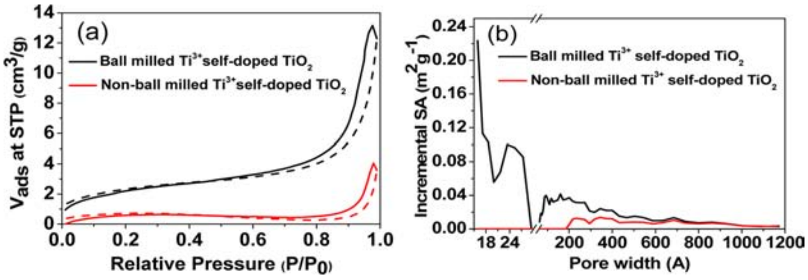

Figure 5. Porosity analysis of photocatalyst. (a) N_2 sorption isotherms at 77 K (solid, desorption; dashed, adsorption). (b) NLDFT pore size distribution for ball-milled (BM) of Ti^{3+}-self-doped TiO_2 samples and nonball-milled (non-BM) Ti^{3+} self-doped TiO_2 samples after being calcinated in Ar at 630 °C for 3 h.

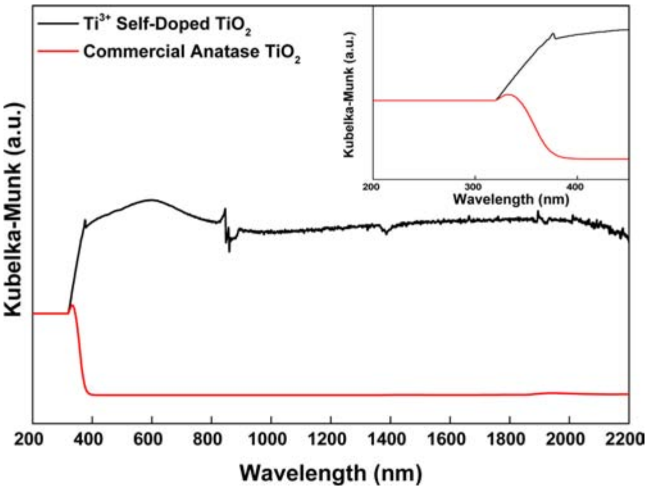

Figure 6. UV−vis-NIR diffuse reflectance spectra of commercial anatase TiO_2 and Ti^{3+} self-doped TiO_2 samples (calcinated at 630 °C). The fringes around 860 nm are due to the change of monochromators. The inset shows the detailed spectrum from 200 to 400 nm.

The photocatalytic activity of the Ti^{3+}-self-doped rutile sample was evaluated by the decomposition of an organic dye molecule under the simulated sun light. Figure 7 shows the UV−vis study of the photocatalytic degradation of 30 mL of a methylene blue aqueous solution (10^{-5} M) using 50 mg of the as-synthesized TiO_2 powders under 1 sun illumination. Within 20 min, the methylene blue molecules were nearly decomposed, evident by the diminishing of the main absorption peak of MB at ~650 nm. To investigate the degree of the photodegradation of MB by our Ti^{3+}-self-doped TiO_2, we conducted an ESI-MS study before and after photodegradation. Figure 8 suggests, during the course of photocatalysis, the MB molecules in water undergo a significant structural degradation with a significant decrease in detectable fragments. The cyclic stability test under the same conditions (Figure 9) showed no significant loss in the photocatalytic activity after six cycles.

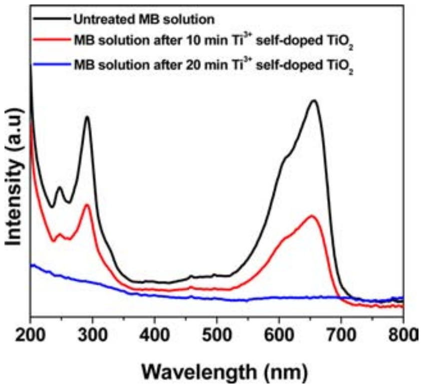

Figure 7. UV−vis absorption spectra of the pure methylene blue (MB) solution before (black line) and after 10 min (red line) and after 20 min (blue line) of solar irradiation in the presence of Ti^{3+}-self-doped TiO_2 calcinated at 630 °C.

To verify that the dye was photodegradated instead of being absorbed on the Ti^{3+}-doped TiO_2 powder, the sample was characterized by FTIR before and after photocatalytic degradation. As is shown in Figure 10, no characteristic IR peaks due to MB is observed on the Ti^{3+}-doped TiO_2 powders after photodegradation. The IR features of the Ti^{3+}-doped TiO_2 powder before and after photocatalytic reaction remains nearly identical. To exclude the possibility that the degradation of MB is due to adsorption on the TiO_2 powder, the photocatalyst was soaked in MB solution for 30 min in the dark followed by the FTIR analysis. The spectrum of the resulting MB shows no identifiable variation when compared to pure MB, indicating there is no degradation of MB in the presence of the photocatalyst in the absence of light.

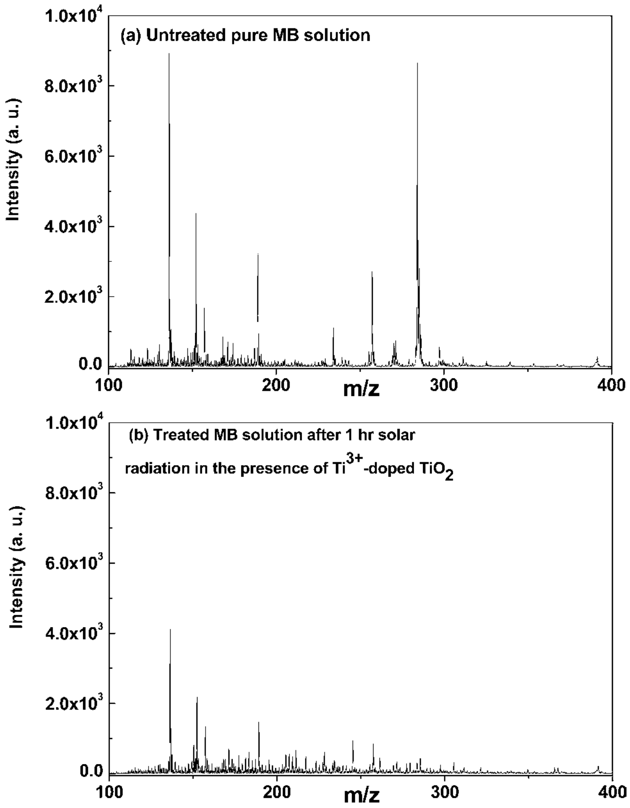

Figure 8. ESI-MS of (a) untreated pure MB solution without photocatalyst present. (b) Treated MB solution after 1 h solar radiation in the presence of Ti^{3+}-doped TiO_2.

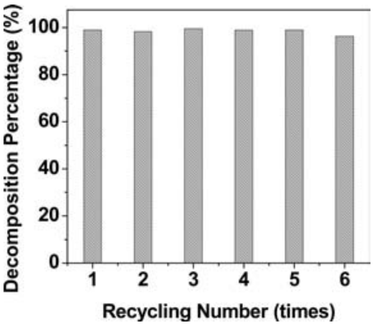

Figure 9. Recycling test results of the Ti^{3+}-self-doped TiO_2 sample being calcinated at 630 °C for 3 h.

To test the feasibility of our Ti^{3+}-self-doped rutile in mitigating organic species in an actual wastewater, we conduct the solar photocatalytic degradation of a colorless industrial wastewater that contains a wide range of unknown organic pollutants (sample obtained from Siemens Water Technology, Rockford, Illinois). Figure 11a and b shows the ESI-MS of the wastewater before and after photocatalytic degradation under 1

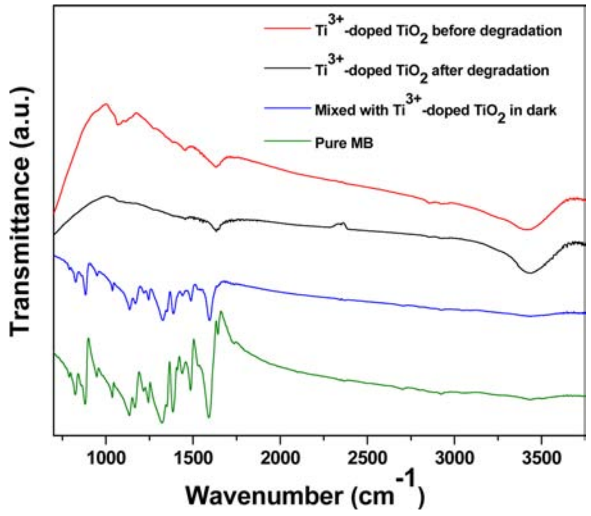

Figure 10. FTIR spectra of Ti^{3+}-doped TiO_2 before photodegradation of methylene blue (red), Ti^{3+}-doped TiO_2 after photodegradation of methylene blue (black), methylene blue after mixed with the Ti^{3+}-doped TiO_2 in the dark (blue), and pure methylene blue (green).

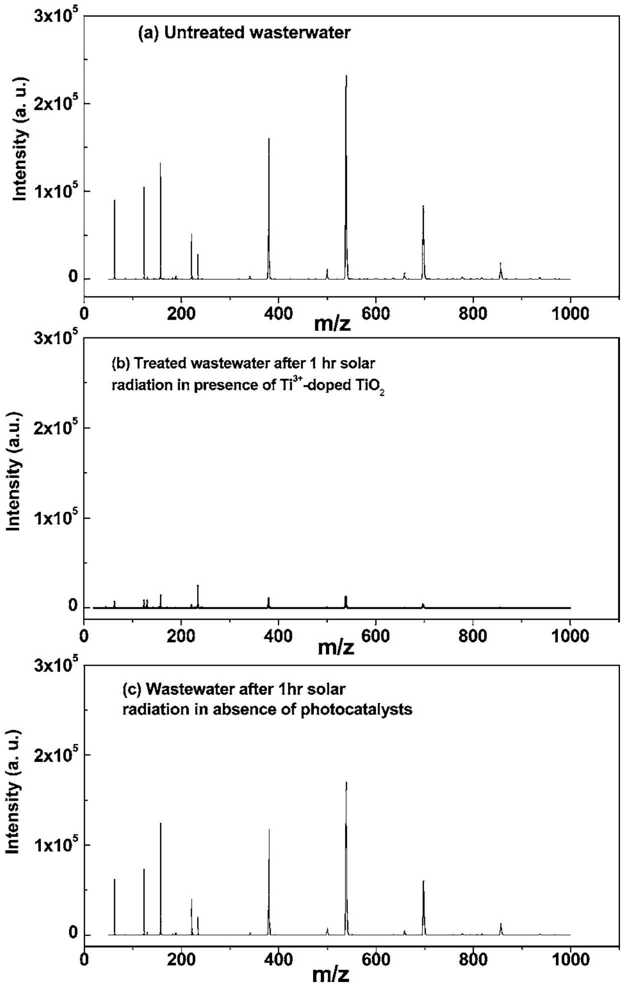

Figure 11. ESI-MS of (a) untreated wastewater with no purification, (b) photodegradated wastewater after 1 h of light irradiation, (c) absence of photocatalyst in wastewater.

sun radiation with a tiny addition of hydrogen peroxide as the source of oxygen (60 mL wastewater + 0.03 g Ti^{3+}-doped TiO_2, and 0.5 mL 30% H_2O_2). After 1 h of solar radiation, the organic pollutants underwent a significant degradation, which is evident by the diminishing of most of the peaks in the mass spectrum of the treated wastewater.

■ CONCLUSIONS

In conclusion, we have developed an economical, scalable, and inorganic chemistry-based method to introduce high-concentration Ti^{3+} (one per ∼4300 Ti^{4+}) in the bulk of rutile TiO_2 via a solution-based oxidation of TiH_2 in H_2O_2, followed by calcinations in Ar. The resulting Ti^{3+}-self-doped TiO_2 showed a high stability in air up to 180 °C. The as-synthesized Ti^{3+}-self-doped TiO_2 also exhibits strong visible-light photocatalytic activity in degradation of organic species in water.

■ AUTHOR INFORMATION

Corresponding Author

*E-mail: txu@niu.edu.

Notes

The authors declare no competing financial interest.

■ ACKNOWLEDGMENTS

T.X. acknowledges the support from National Science Foundation (CBET-1150617). The electron microscopy was conducted at the Electron Microscopy Center for Materials Research at Argonne National Laboratory, a U.S. Department of Energy Office of Science Laboratory operated under Contract No. DE-AC02-06CH11357 by U of Chicago Argonne, LLC. D.J.L. also thanks the support by the U.S. Department of Energy under contract No. DE-AC02-06CH11357. Use of the Center for Nanoscale Materials was supported by the U.S. Department of Energy, Office of Science, Office of Basic Energy Sciences, under Contract No. DE-AC02-06CH11357. We also thank Dr. Xiao-Min Lin for technique support on UV−vis-NIR measurement.

■ REFERENCES

(1) Hoffmann, M. R.; Martin, S. T.; Choi, W. Y.; Bahnemann, D. W. *Chem. Rev.* **1995**, *95*, 69−96.

(2) Linsebigler, A. L.; Lu, G. Q.; Yates, J. T. *Chem. Rev.* **1995**, *95*, 735−758.

(3) Thompson, T. L.; Yates, J. T. *Chem. Rev.* **2006**, *106*, 4428−4453.

(4) Alvaro, M.; Aprile, C.; Benitez, M.; Carbonell, E.; Garcia, H. *J. Phys. Chem. B* **2006**, *110*, 6661−6665.

(5) He, D. P.; Lin, F. R. *Mater. Lett.* **2007**, *61*, 3385−3387.

(6) Finazzi, E.; Di Valentin, C.; Pacchioni, G. *J. Phys. Chem. C* **2009**, *113*, 220−228.

(7) Gopal, N. O.; Lo, H. H.; Ke, S. C. *J. Am. Chem. Soc.* **2008**, *130*, 2760−2761.

(8) Periyat, P. P., S. C.; McCormack, D. E.; Colreavy, J. *J. Phys. Chem. C* **2008**, *112*, 7644−7652.

(9) Periyat, P. M., D. E.; Hinder, S. J.; Pillai, S. C. *J. Phys. Chem. C* **2009**, *113*, 3246−3253.

(10) Hamal, D. B.; Klabunde, K. J. *J. Colloid Interface Sci.* **2007**, *311*, 514−522.

(11) Zheng, Z. K.; Huang, B. B.; Y., Q. X.; Zhang, X. Y.; Dai, Y.; Whangbo, M. H. *J. Mater. Chem.* **2011**, *21*, 9079−9087.

(12) Xu, P.; Lu, J.; Xu, T.; Gao, S.; Huang, B.; Dai, Y. *J. Phys. Chem. C* **2010**, *114*, 9510−9517.

(13) Xu, P.; Xu, T.; Lu, J.; Gao, S.; Hosmane, N. S.; Huang, B.; Dai, Y.; Wang, Y. *Energy Environ. Sci.* **2010**, *3*, 1128−1134.

(14) Asahi, R.; Morikawa, T.; Ohwaki, T.; Aoki, K.; Taga, Y. *Science* **2001**, *293*, 269.

(15) Zuo, F.; Wang, L.; Wu, T.; Zhang, Z.; Borchardt, D.; Feng, P. *J. Am. Chem. Soc.* **2010**, *132*, 11856−11857.

(16) Chen, X.; Liu, L.; Yu, P. Y.; Mao, S. S. *Science* **2011**, *331*, 746−750.

(17) Zuo, F.; Bozhilov, K.; Dillon, R. J.; Wang, L.; Smith, P.; Zhao, X.; Bardeen, C.; Feng, P. *Angew. Chem., Int. Ed. Engl.* **2012**, *51*, 6223−6226.

(18) Hoang, S.; Berglund, S. P.; Hahn, N. T.; Bard, A. J.; Mullins, C. B. *J. Am. Chem. Soc.* **2012**, *134*, 3659−3662.

(19) Wang, W.; Ni, Y.; Lu, C.; Xu, Z. *RSC Adv.* **2012**, *2*, 8286−8288.

(20) Justicia, I.; Ordejon, P.; Canto, G.; Mozos, J. L.; Fraxedes, J.; Battiston, G. A.; Gerbasi, R.; Figueras, A. *Adv. Mater.* **2002**, *14*, 1399−1402.

(21) Nowotny, J.; Bak, T.; Nowotny, M. K.; Sheppard, L. R. *J. Phys. Chem. B* **2006**, *110*, 18492−18495.

(22) Cronemeyer, D. C. *Phys. Rev.* **1959**, *113*, 1222−1226.

(23) Teleki, A.; Pratsinis, S. E. *Phys. Chem. Chem. Phys.* **2009**, *11*, 3742−3747.

(24) Komaguchi, K.; Maruoka, T.; Nakano, H.; Imae, I.; Ooyama, Y.; Harima, Y. *J. Phys. Chem. C* **2010**, *114*, 1240−1245.

(25) Kennedy, A. R.; Lppez, V. H. *Mater. Sci. Eng.* **2003**, *A357*, 258−263.

(26) Anderson, K.; Fleshman, W. S. *Ind. Eng. Chem.* **1950**, *42*, 1381−1383.

(27) Murakami, N.; Katayama, S.; Nakamura, M.; Tsubota, T.; Ohno. *J. Phys. Chem. C* **2011**, *115*, 419−424.

(28) Deskins, N. A.; Rousseau, R.; Dupuis, M. *J. Phys. Chem. C* **2011**, *115*, 7562−7572.

(29) Hurum, D. C.; Agrios, A. G.; Gray, K. A.; Rajh, T.; Thurnauer, M. C. *J. Phys. Chem. B* **2003**, *107*, 4545−4549.

(30) Hurum, D. C.; Gray, K. A.; Rajh, T.; Thurnauer, M. C. *J. Phys. Chem. B* **2005**, *109*, 977−980.

(31) Howe, R. F.; Gratzel, M. *J. Phys. Chem.* **1985**, *89*, 4495−4499.

(32) Berger, T.; Sterrer, M.; Diwald, O.; Knozinger, E.; Panayotov, D.; Thompson, T. L.; Yates, J. T. *J. Phys. Chem. B* **2005**, *109*, 6061−6068.

(33) Cunningh., J.; Penny, A. L. *J. Phys. Chem.* **1974**, *78*, 870−875.

(34) Zhang, J.; Zhang, Y.; Y., Y. L.; Pa, C. *Catal. Sci. Technol.* **2011**, *1*, 273−278.

(35) Zhu, G.; Pan, L.; Xu, T.; Sun, Z. *ACS Appl. Mater. Interfaces* **2011**, *3*, 3146−3151.

(36) Bakardjieva, S.; Subrt, J.; Stengl, V.; Dianez, M. J.; Sayagues, M. J. *Appl. Catal. B−Envrion.* **2005**, *58*, 193−202.

(37) Almquist, C. B.; Biswas, P. *J. Catal.* **2002**, *212*, 145−156.